Transiently delocalized states enhance hole mobility in organic molecular semiconductors

Samuele Giannini*[1#], Lucia Di Virgilio[2#], Marco Bardini[1], Julian Hausch[3], Jaco J. Geuchies[2], Wenhao Zheng[2], Martina Volpi[4], Jan Elsner[6], Katharina Broch[3], Yves H. Geerts[4,5], Frank Schreiber[3], Guillaume Schweicher[4], Hai I. Wang*[7], Jochen Blumberger[6], Mischa Bonn*[2], David Beljonne*[1]

[1] Laboratory for Chemistry of Novel Materials, University of Mons, Mons 7000, Belgium

[2] Max Planck Institute for Polymer Research, Ackermannweg 10, 55128, Mainz, Germany

[3] Institut für Angewandte Physik, Universität Tübingen, Auf der Morgenstelle 10, 72076 Tübingen, Germany

[4] Laboratoire de Chimie des Polymères, Faculté des Sciences, Université Libre de Bruxelles (ULB), Boulevard du Triomphe, CP 206/01, 1050 Bruxelles, Belgium

[5] International Solvay Institutes for Physics and Chemistry, Université Libre de Bruxelles (ULB), Boulevard du Triomphe, CP 231, 1050 Bruxelles, Belgium

[6] Department of Physics and Astronomy and Thomas Young Centre, University College London, London WC1E 6BT, UK

[7] Nanophotonics, Debye Institute for Nanomaterials Science, Utrecht University, Princetonplein 1, 3584 CC Utrecht, The Netherlands

*Correspondence to: david.beljonne@umons.ac.be , bonn@mpip-mainz.mpg.de, h.wang5@uu.nl, samuele.giannini@umons.ac.be

#These authors contributed equally to this work

Abstract

Evidence shows that charge carriers in organic semiconductors (OSs) self-localize because of dynamic disorder. Nevertheless, some OSs feature reduced mobility at increasing temperature, a hallmark for delocalized band transport. Here we present the temperature-dependent mobility in two record-mobility OSs: DNTT (dinaphtho[2,3-b:2′,3′-f]thieno[3,2-b]-thiophene), and its alkylated derivative, C8-DNTT-C8. By combining terahertz photoconductivity measurements with atomistic non-adiabatic molecular dynamics simulations, we show that while both crystals display a power-law decrease of the mobility (μ) with temperature (T, following: $\mu \propto T^{-n}$), the exponent n differs substantially. Modelling reveals that the differences between the two chemically similar semiconductors can be traced to the delocalization of the different states thermally accessible by charge carriers, which in turn depends on their specific electronic band structure. The emerging picture is that of holes surfing on a dynamic manifold of vibrationally-dressed extended states with a temperature-dependent mobility that provides a sensitive fingerprint for the underlying density of states.

Recent computational[1–4] and experimental[5–9] studies on molecular semiconductors have provided compelling evidence that charge carriers (holes or electrons) form partially delocalized quantum objects "half way" between waves and particles. Thermal disorder between the weakly bound molecules in these molecular systems prevents full wave-like delocalization, while sizable electronic couplings (H_{kl}, where k and l represent two interacting molecules) and small nuclear reorganization energies (λ) prevent full localization.[1,10] Several experimental investigations (by time-of-flight,[11] Hall effect,[12,13] space-charge-limited current[14], and transient photoconductivity measurements[15]), conducted on high-mobility low-disorder single-crystal organic semiconductors have reported increasing mobility with decreasing temperature, following a power law relation $\mu \propto T^{-n}$ with n ranging from ~0.5 to ~3. The reason for the large span in n values is, however, unclear.

On the theoretical front, the so-called "Transient Localization Scenario",[2,4,16] has been developed to understand the intriguing dichotomy between extended and localized states concomitantly contributing to the thermally accessible band spectrum.[2,17] Localized states form preferentially at the band edges. Still, the charge carriers can undergo transient quantum delocalization owing to thermal disorder, provided that higher-energy extended states are thermally accessible to enable these dynamic excursions. This is reminiscent of the mobility edge theory,[18] but in a dynamic energy landscape due to nuclear motion (mostly low-frequency crystal phonons involving the rigid-body motion of the interacting molecules). Fratini *et al.* formalized this picture in the so-called transient localization theory (TLT).[2,16,19,20] By assuming the relaxation time approximation,[2] the authors derived a simple analytical formula in which the mobility is directly proportional to the (square of the) carrier localization length and inversely proportional to the temperature and to the fluctuation time (which depends on the period of intermolecular oscillations). Although TLT has been successfully applied to reconcile many experimental features of OSs and to derive design rules for the discovery of high-mobility OSs,[20,21] many subtleties of charge transport in OSs remain enigmatic.

Here, by combining non-adiabatic molecular dynamics simulations,[4,22–25] in the framework of the atomistic fragment orbital-based surface hopping (FOB-SH),[4,25,26] with ultrafast THz spectroscopy, we show how two representative high-mobility OSs (namely DNTT and its alkylated derivative, C8-DNTT-C8) that only differ by the presence of alkyl side chains, feature marked differences in their *T*-dependent charge carrier mobility. The use of efficient numerical approaches to solve the electronic time-dependent Schrödinger equation coupled to the nuclear motion, combined with advanced terahertz conductivity measurements, provides atomistic resolution in understanding structure-property relationships.

DNTT and C8-DNTT-C8 are among the best-performing molecular OSs with charge carrier mobility up to 8-11 cm^2 V^{-1} s^{-1} in field-effect transistors.[27–29] Several experimental and theoretical studies have been devoted to DNTT,[30–33] and, more recently, also C8-DNTT-C8.[29] Both materials benefit from a favourable 2D charge transport character within the herringbone layer (see **Fig. 1**) and reduced dynamic disorder, which favours large wavefunction delocalization and high charge carrier mobilities.[29] Surprisingly, few studies have been devoted to their temperature-dependent mobility. In DNTT, the charge carrier mobility measured in OFETs was almost *T*-independent,[34,35] a result seemingly at odds with the band-like behaviour expected for such a high-mobility semiconductor.

We report below an unforeseen relationship between the temperature-dependent mobility and the electronic structure topology of these two OSs. In both molecular materials, our combined experimental-theoretical investigations show that the carrier mobility increases as the temperature decreases from 400 to 78 K, yet at a rate significantly higher in C8-DNTT-C8 than DNTT. Our modelling reveals that such a different evolution is driven by distinctive features in their electronic band structures, namely the different relative signs of the couplings and the degree of in-plane coupling anisotropy. In DNTT, this results in relatively localized tail states at the top of the valence band featuring similar extensions at varying temperatures. In contrast, C8-DNTT-C8 shows increasingly delocalized states at the valence band edge as the temperature decreases. As a result, charge carriers can thermally access more extended states giving rise to a higher mobility in C8-DNTT-C8, particularly at lower temperatures, hence the stronger falloff of μ with T (as confirmed by THz measurements).

Photo-induced conductivity of DNTT and C8-DNTT-C8. We employ contact-free THz spectroscopy on polycrystalline films of DNTT and C8-DNTT-C8 deposited on fused silica substrate (see information in Supplementary Figs. 1 to 3). Optical pump-THz probe (OPTP) experiments allow optical injection of charge carriers by a fs laser pulse, and probing of the transient photoconductivity by a THz pulse (with bandwidth up to ~2 THz).[36,37] Photogenerated free charge carriers in OSs absorb THz radiation, resulting in an attenuation (ΔE) of the transmitted THz field E. The photoconductivity σ can be inferred from $\sigma \propto -\Delta E/E$, using the thin-film approximation (Eq. 1).[38,39] The time evolution of σ can be tracked as a function of pump-probe delay with sub-ps time resolution, and is proportional to $\phi\mu$ (the product of carrier mobility μ and free carrier generation quantum yield ϕ; see details in caption in **Fig. 2**). A detailed description of OPTP spectroscopy is included in the Methods section and Supplementary Note 2.

We conducted T-dependent photoconductivity measurements in the range 78-300K (Fig. 2b,c). At any given T, the photoconductivity (normalized by the number of absorbed photons per volume), or equivalently $\phi\mu$ in both samples builds up in ~1 ps, and lives for more than 1 ns following a minor decay in the first 10 ps (see Supplementary Fig. 4). Two important conclusions can be immediately drawn. First, at room temperature (RT), C8-DNTT-C8 displays a substantially higher photoconductivity than DNTT (by a factor of ~ 1.5, see data in Fig. 2 and Supplementary Fig. 5), in agreement with Ref.[29]. Second, the photoconductivity (and hence carrier mobility) of both materials increases with decreasing temperature, suggesting a band-like transport. While this T-dependent photoconductivity trend is barely visible in DNTT, it is very pronounced in C8-DNTT-C8 (at 78 K, the mobility is 3 times larger than at RT), irrespective of the film thickness (see Supplementary Figs. 5, 6 and Fig. 7a,b).

To obtain further insights into the T-dependent photoconductivity in Fig. 2b,c, we recorded complex frequency-resolved photoconductivity at various T (at a fixed pump-probe delay of ~0.5 ps). In the T range studied, the photoconductivity is dominated by the real part of the conductivity (see **Fig. 3**), indicating that free carrier conduction dominates the terahertz photoresponse.[36] Most notably, at odds with a pure Drude-like response,[40] the real part of the photoconductivity increases with frequency: a characteristic hallmark of transient localization of the charge carrier induced by

dynamic disorder.[19,41] Such behaviour has been observed previously in rubrene, by both field-effect transistor and photoconductivity studies.[42–44]

Fratini *et al.* derived an important phenomenological Drude-Anderson (DA) model,[41] to interpolate between the Drude-like response of diffusive carriers and the finite-frequency peak expected for Anderson localization. Details of the model are given in the Methods section. A perfectly adequate description of the photoconductivity data using the DA model can be obtained assuming temperature-independent inelastic scattering time τ_{in} (see Methods and Supplementary Fig. 9a,b). From the DA fitting we find that h/τ_{in} is around 9 meV for DNTT and 16 meV for C8-DNTT-C8 in the typical range of other OSs.[16,45] These values are also in line with the related time scale found by computing the power spectral density of the coupling fluctuations (see Supplementary Fig. 27). The fitting procedure yields T-independent elastic scattering time, τ (h/τ of 198 meV and 300 meV) and the backscattering time, τ_b (h/τ_b of 20 meV and 30 meV) for DNTT and C8-DNTT-C8, respectively (see Supplementary Fig. 9).

Transport parameters and thermal disorder. We start our computational analysis by evaluating transport parameters, *i.e.*, internal reorganization energies (λ) and electronic couplings (H_{kl}) within the herringbone layer crystal structure of DNTT and C8-DNTT-C8 (Fig. 1c). Cell parameters are given in Supplementary Table 1. We note that the two systems show similar unit-cell areas, which is important for a one-to-one comparison between the two (*e.g.* the absolute mobility is proportional to the square of the lattice spacing[21]). However, the presence of the alkyl side chains has an impact on the molecular packing of the two systems, as described in Supplementary Note 24. We refer to Supplementary Notes 8 and 9 for a description of the DFT calculations performed for reorganization energies and electronic couplings (see Fig. 1a,b and Table 1). Note that in both systems, holes are more mobile than electrons and should represent the majority carriers probed by our OPTP measurements (see Supplementary Note 12). We show that in both DNTT and C8-DNTT-C8, hole-transfer couplings are sizable, exceeding half of the reorganization energy for some of the closest nearest-neighbour pairs ($H_{kl} > \lambda/2$). In this regime, charges can delocalize over multiple molecules. Consequently, small polaron hopping model breaks down.[1,10] This is the first important observation defining high-mobility OSs.[3,4] Thus, alternative transport theories (*e.g.* TLT) or direct numerical approaches (*e.g.* FOB-SH) are called for. We also note that in this regime, the delocalization of the charge is limited by the strength of both local and non-local electron-phonon couplings.[3] To explicitly account for dynamic thermal disorder, we evaluate the time-dependent Hamiltonian (Eq. 5) along FOB-SH trajectories by explicitly calculating both diagonal and off-diagonal elements on-the-fly (see Supplementary Note 14). We find that both DNTT and C8-DNTT-C8 show relatively small coupling fluctuations compared to their mean values ($V = \langle H_{kl} \rangle$), especially in P_a direction (where σ_V is about 4-5 times smaller than V). The small thermal disorder partly explains the large mobilities in these materials.[29] We also find that site energy fluctuations, as well as electronic coupling fluctuations, increase with increasing temperature ($\sigma_{\Delta E(V)} \propto \sqrt{T}$) as expected for an increased thermal disorder, in line with the situation in other OSs.[46]

Coupling-sign relationship and band structure anisotropy. The transient localization framework[20] predicts that in molecular semiconductors characterized by a 2D herringbone layer packing, the shape of the density of states (DOS) as well as the degree of localization of the states at the top of the valence band (or at the bottom of the conduction band) is intimately related to the sign combination and relative magnitude of the three largest nearest-neighbour electronic transfer integrals. For holes, a positive product of "signed" nearest-neighbour couplings (in the following referred to as "positive coupling-sign relation"), in combination with isotropic electronic couplings (*i.e.*, similar in magnitude), yield large carrier delocalization and, thus, fast hole carrier transport. The opposite is valid for electron transfer systems. The same conclusions can be drawn from explicit numerical propagation of the wavefunction using FOB-SH non-adiabatic dynamics.[4,47]

In this respect, C8-DNTT-C8 features a positive coupling-sign relationship when considering the nearest-neighbour hole transfer couplings (see Fig. 1b), and exhibits only weak anisotropy in electronic couplings within the conductive herringbone layer (see Fig. 1c). In contrast, DNTT yields an unfavourable combination (see Fig. 1a) with a negative coupling-sign relation for hole transfer (*i.e.*, a negative product of signed nearest-neighbour couplings) and a high degree of anisotropy. The consequences on the band structure of these two materials are already visible when computing the DOS for the frozen crystals at 0 K (black line in Supplementary Fig. 17). Interestingly, while the DOS of DNTT peaks at the top of the valence band, it peaks at the bottom of the corresponding band in C8-DNTT-C8. This outcome directly results from the phase relationship between interacting hole wavefunctions in the herringbone plane. It significantly affects the spatial extension of the states and their mobility with temperature, as explain below.

Delocalization of the states. The time-dependent electronic Hamiltonian (Eq. 5) computed at each time-step along non-adiabatic dynamics trajectories can be diagonalized to investigate the effect of temperature and coupling-sign relationship on both the DOS and the localization of the valence band states in DNTT and C8-DNTT-C8. Looking at the top panels in **Fig. 4**, we can see that the DOS of both materials increasingly broadens with increasing thermal disorder, *i.e.,* a larger number of tail states appear at higher temperatures (see Supplementary Fig. 17). In the bottom panels of Fig. 4, we superimpose the DOS with the inverse participation ratio IPR$_i$, defined in Eq. 8, averaged over trajectory and time-steps for a given state, i, yielding $\langle IPR_i \rangle_C$. This quantity is related to the number of molecules over which state i is delocalized. The larger $\langle IPR_i \rangle_C$, the more delocalized (on average) the states that the charge carrier can thermally access. Thus, this figure depicting an IPR-resolved DOS, gives information about the spatial extent of the valence band states as a function of their energy. In DNTT (Fig. 4a-c), we can observe that, at all temperatures, the top of the valence band is formed by a dense manifold of relatively localized states. This delocalization can be quantified by a Boltzmann average of the states IPR$_i$, $\langle IPR \rangle_B \approx 30$ at 300 K (horizontal dashed red line). The most delocalized states, which are thermally inaccessible around RT, are instead localized in the middle of the valence band at $E \approx$ -600 meV ($\langle IPR_i \rangle_C \approx 200$ at 300 K). Strikingly, in C8-DNTT-C8 (Fig. 4d-f), the pattern of states (de)localization is inverted. Thermally accessible states with a very high delocalization are now found at the top of the valence band, within a few $k_B T$ of the band edge (*e.g.*, $\langle IPR \rangle_B \approx 80$ at 300 K, horizontal dashed red line). A dense manifold of localized states is instead predicted at the bottom of the valence band. This is

a remarkable consequence of the sign combination, which is favourable (positive coupling-sign relation) for C8-DNTT-C8 but not for DNTT.

Temperature-dependent charge carrier mobility. We now turn to the main outcome of this work, namely the comparison between the simulated and measured temperature dependence of the mobility in DNTT versus C8-DNTT-C8. We extracted the dc conductivity from frequency-resolved conductivity spectra, and the related mobility based on the DA model (see Methods). Our analysis, in **Fig. 5,** reveals that the mobility follows a power law dependence, $\mu \propto T^{-n}$, with $n = 0.5 \pm 0.1$ in DNTT and $n = 1 \pm 0.1$ in C8-DNTT-C8. According to the DA model, such power laws are a consequence of the joint effect of the factor T^{-1} in the mobility expression in Eq. 4 and the temperature dependence of the diffusion coefficient (D), related to L^2 by $D \cong \frac{L^2}{2\tau_{in}}$. In Supplementary Fig. 10, we show that D is roughly temperature independent in C8-DNTT-C8, yielding an overall T^{-1} mobility temperature dependence. In contrast, D in DNTT is weakly thermally activated, explaining the smaller power law exponent for μ in DNTT compared to C8-DNTT-C8. From this analysis, we also found that charges in C8-DNTT-C8 travel larger distances as they are characterized by a squared localization length, L^2, of about 600 $Å^2$. While, for DNTT, L^2 is about 400 $Å^2$ at RT (see Methods section for details). To confirm the DA fitting results, we directly use the T-dependent photoconductivity data normalized to the absorbed photon density, $\phi\mu$ (Eq. 1), as shown in Fig. 2b,c. Our analysis unveils that $\phi\mu$ also follows a power law dependence, with $n = 0.26 \pm 0.05$ in DNTT and $n = 0.77 \pm 0.08$ in C8-DNTT-C8, respectively (see Supplementary Fig. 8). The change in μ dominates the $\phi\mu$ modulation as ϕ is found to be weakly T-dependent (see Supplementary Table 1). This independent analysis is thus fully consistent with the DA analysis.

To rationalize the experimental temperature-dependent data, we run a swarm of FOB-SH non-adiabatic dynamics trajectories at various temperatures. The mean squared displacement (MSD) of the wavefunction $\Psi(t)$ is evaluated with (Eq. 11), and we also quantified the delocalization of $\Psi(t)$ using the average IPR (Eq. 9) (see Methods).[47,48] From the calculated MSD we can extract first the diffusion coefficients and then the mean plane values $\mu_{\langle ab \rangle} = (\mu_a + \mu_b)/2$ of the charge carrier mobility for both DNTT and C8-DNTT-C8, using the Einstein relation (Eq. 10)[47,48]. The computed values were evaluated in the temperature range between 150 K and 400 K (see Fig. 5a,b), where nuclear quantum effects are expected to be relatively small (specifically, since electronic couplings are considerable and tunneling barriers along the main transport directions are not present).[49] The simulated mobility of C8-DNTT-C8 is about 3 times higher than in DNTT at RT. This observation agrees quantitatively with the OPTP results (see Fig. 5), and with previously reported literature OFET mobility values.[29] Additionally, as shown in Supplementary Fig. 25, for DNTT, the degree of transport anisotropy in the a and b crystallographic directions given by our simulations ($\mu_a/\mu_b \approx 1.5 - 2.0$, depending on the temperature) is consistent with previous theoretical estimates[31] as well as other experimental OFETs mobility measurements ($\mu_a/\mu_b \approx 1.3 - 1.7$).[34]

Non-adiabatic dynamics simulations confirm our previous experimental observation that while C8-DNTT-C8 features an almost T-independent D, DNTT shows a weakly activated D

(Supplementary Fig. 10a,b). Computed mobilities (Fig. 5a,b) in these two systems scale with power-law exponents of $n = 0.38 \pm 0.08$ and $n = 0.83 \pm 0.06$ for DNTT and C8-DNTT-C8, respectively, in line with the experimental results. The remaining differences, *e.g.*, the discrepancies in the computed power-law with respect to temperature and the absolute mobilities compared to experiment could be due to several factors not included in the model, such as the presence of residual static defects or molecular misalignment, as well as inherent limitations of the computational method. Despite these residual uncertainties, both experiment and computation agree on the higher RT mobility (*i.e.*, factor ~3) and the steeper power-law scaling of C8-DNTT-C8 vs. DNTT.

Outlook

The answer to the question of the origin of the higher RT mobility, and the steeper power-law dependence in C8-DNTT-C8 compared to DNTT can be found in the transient quantum (de)localization mechanism mediating charge transport.[4,25] At 300 K, the charge carrier wavefunction, $\Psi(t)$, is delocalized over 65 and 22 molecules in C8-DNTT-C8 and DNTT, respectively. The average size of the charge carrier, $\langle IPR \rangle$, (Eq. 9) represented with yellow dots in Fig. 5c,d), aligns well with the extension of thermally accessible states at a given temperature,[50] quantified using the Boltzmann average IPR, $\langle IPR \rangle_B$ (see Methods).

Notably, though $\Psi(t)$ is a finite-size charge carrier – on average over the entire swarm of FOB-SH trajectories – each individual trajectory reveals that the charge carrier is essentially a highly dynamical "flickering" object with the tendency to delocalize over an even larger number of molecules with respect to its average (see skewed IPR distribution in Fig. 5c,d). By following the typical evolution of $\Psi(t)$ at different temperatures, we find that, in several instances (shaded regions in Supplementary Fig. 18), this undergoes transient (short-lived) thermal intra-band excitations that bring $\Psi(t)$ from relatively localized tail states to more delocalized states closer to the middle of the valence band (see Fig. 4). Such transient expansions of the wavefunction, by which the charge carrier can "surf" highly delocalized electronic states, drive the wavefunction displacement to longer distances. Importantly, the more extended the thermally accessible *hole* eigenstates at the top of the valence band, the higher the wavefunction delocalization and possible long-range displacement that the charge on average can undergo (thereby leading to larger MSDs and mobility values). However, the access to more spatially delocalized states at lower temperatures is partly compensated by the reduced thermal energy available to surf over such states (see Supplementary Fig. 22).

In Fig. 5c,d we show that: the IPR distribution (at all temperatures) is shifted to higher IPR values in C8-DNTT-C8 as compared to DNTT, and thermally accessible delocalized valence band states, as in the case of C8-DNTT-C8, favour a much broader tail at larger IPRs forming a right-skewed distribution. These characteristics underpin the more effective transient (de)localization mechanism occurring in C8-DNTT-C8 and, thus, the larger mobility found in this system compared to DNTT (see discussion in Supplementary Note 16). In particular, in Fig. 5c,d, we observe that the average IPR of $\Psi(t)$ decreases more strongly in C8-DNTT-C8 than in DNTT, qualitatively tracking the steepness of the mobility falloff with temperature in the two systems. With decreasing temperature, in C8-DNTT-C8, the IPR distributions become skewed comparably

more strongly towards higher IPR values than in DNTT. This means that the transient delocalization mechanism, ruling spatial displacements and mobility, is expected to become comparably more efficient in C8-DNTT-C8 than in DNTT upon lowering the temperature. Remarkably, these results can be traced to the shape of the state-resolved IPR reported in Fig. 4 (see Supplementary Note 16). By zooming into the tail of the thermally accessible states at different temperatures, as shown in Supplementary Fig. 20, we can see how the slope of the top valence band-edge states (within a few k_BT) is much steeper in C8-DNTT-C8 compared to DNTT. In C8-DNTT-C8, thermally accessible states become consistently more delocalized with decreasing temperature than in DNTT. This larger delocalization partially offsets the energy penalty introduced by decreasing the thermal energy available for the carrier wavefunction to access those states (see Supplementary Fig. 22). Thus, we argue that a favourable coupling-sign combination, as in the case of C8-DNTT-C8, is not only important for producing extended thermally accessible states which yield higher mobilities, but also favours an increasingly steeper slope of delocalized states at lower temperatures. In other words, the shape of the state-resolved delocalized density of states (which in turn depends on temperature, static and dynamic disorder, the strength of electron-phonon interactions, coupling-sign relation, etc.) arguably provides a fingerprint of the mobility temperature dependence for these two high-mobility systems. We remark that these effects cannot be captured by standard theories such as hopping models or semiclassical band transport (see Supplementary Note 18).

The considerations made in this work likely apply more broadly to other high-mobility OSs (where $H_{kl} > \lambda/2$), though the trends might be somewhat blurred by other effects (amount of thermal disorder, unit-cell area, the magnitude of the reorganization energy, sample purity, etc.). In Supplementary Fig. 26, we consider the two best-known OSs, pentacene and rubrene, and their experimental temperature-dependence mobilities. In pentacene, where the relative coupling-sign relationship within their herringbone planes is negative (as for DNTT), the power law factor tends to be generally smaller than for rubrene for which the coupling-sign relationship is positive (as for C8-DNTT-C8). The experimental RT mobility of pentacene is also lower than that of rubrene, echoing the comparison of DNTT and its alkylated derivative. These observations underline that the transient (de)localization mechanism at play is affected differently by the different underlying band structure features of the given OS (in addition to other electronic and structural properties).

In OSs where the charge is fully localized by strong local-electron phonon interactions (*i.e.*, low-mobility OSs), the interference effects that made the relative sign of the coupling important gradually becomes less relevant as one expects for pure hopping transport, and other effects might become dominant. For instance, Shuai and co-workers showed that nuclear quantum effects substantially increase the transport rates, especially for systems with large λ.[51,52] Therefore, OSs with high activation energy barrier ($\Delta A^{\ddagger} = \lambda/4$) are likely subject to a comparably stronger increase of the mobility at lower temperature than at RT due to the possibility for the charge to tunnel through the activation barrier (tunnelling effects become less relevant at RT[49]). In addition, in the hopping regime, where the TLT assumptions break down, non-local electron-phonon coupling might enhance mobility through a phonon-assisted transport mechanism as predicted by Munn-Silbey theory[53,54] and further demonstrated by explicit non-adiabatic dynamics as well.[55]

In conclusion, our work provides a comprehensive description of charge transport in two record-mobility OSs, *i.e.* DNTT and C8-DNTT-C8, emphasizing how seemingly small changes in chemical structure profoundly impact their T-dependent charge-carrier mobility. We also highlight the remarkable agreement between experiment and theory as a definite demonstration that charge transport in high-mobility molecular semiconductors proceeds through a transient (de)localization mechanism at the foundation of their different power law factors. In particular, we have shown that in DNTT and its alkylated derivative, which feature similar structure, lattice spacing, average couplings, and even coupling fluctuations, the mobility and, importantly, the T-dependence of the mobility can be significantly different. This difference can be traced to different sign combinations and degree of anisotropy of the largest nearest-neighbour couplings within the herringbone layers of these systems. While the importance of these two characteristics has been appreciated before for absolute mobilities in the context of transient localization theory, this is, to our knowledge, the first time that their relevance to T-dependent mobility of the charge carriers has been directly and quantitatively established using experiment and simulation.

Acknowledgements

Author contributions

S.G. performed most of the quantum chemical calculations presented in this work and performed related data analysis (with input from J.E. and M.Bar.). M.Bar. and S.G. ran non-adiabatic dynamics simulations of charge transport for the systems investigated in this work. L.D.V conducted the terahertz spectroscopy experiments and analyzed the data together with M.Bar J.J.G. J.H. and K.B. prepared samples. L.D.V and S.G. also performed the analysis of the experimental data using the Drude-Anderson model. M.V. synthesized C8-DNTT-C8. G.S. contributed to sample preparation and data interpretation. J.J.G. performed XRD measurements. M.Bonn and Y.G. initiated the experimental study of charge transport in thienoacene semiconductors, at short length- and time-scales. D.B. J.B. H.I.W. F.S. and M.Bonn contributed to the data interpretation and D.B., H.I.W, and M.Bonn supervised all aspects of the research. S.G., L.D.V, H.I.W. and D.B. designed the research and wrote the manuscript. All authors reviewed and discussed the manuscript.
.

Competing interests

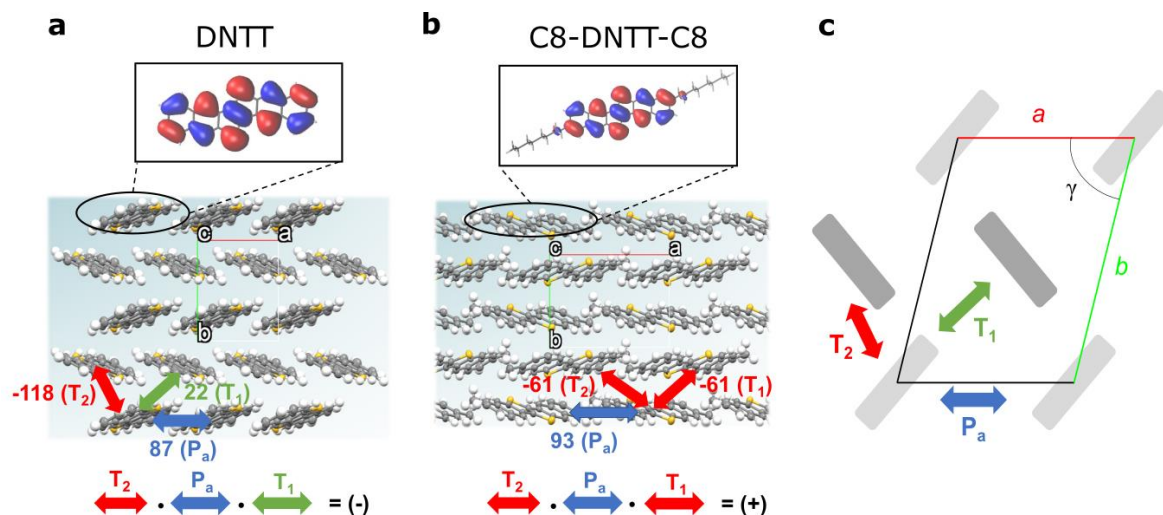The authors declare no competing interests.

Figure 1: Molecular herringbone layer packing for the investigated OSs. The three strongest nearest-neighbor couplings are represented in the *a-b* plane of **(a)** DNTT and **(b)** C8-DNTT-C8 (alkyl side chains have been replaced by methyl groups for clarity). The DFT highest occupied molecular orbital (HOMO) of single molecules are depicted as isosurfaces for both systems. The positive (negative) coupling-sign relationship characterizing C8-DNTT-C8 (DNTT), is represented by colored arrows and described in detail in the text (same colors have been used for equivalent coupling values). **(c)** Representation of a general two-dimensional unit cell. In all panels the unit cell axes *a, b* are shown in red and green, respectively (axis *c* is eclipsed by the other two).
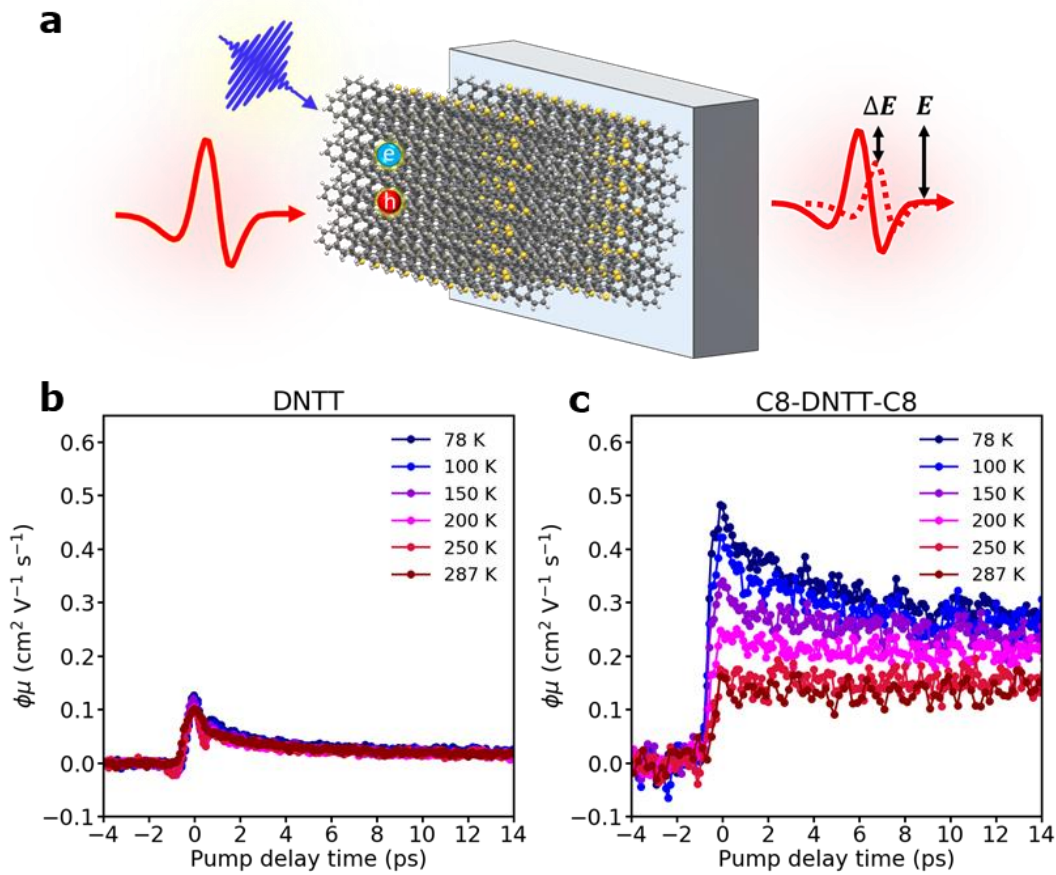
Figure 2: *T*-dependent photoconductivity studies by optical-pump THz-probe (OPTP) spectroscopy in DNTT and C8-DNTT-C8. **(a)** Schematic illustration of the OPTP spectroscopy. Photoconductivity dynamics of **(b)** DNTT and **(c)** C8-DNTT-C8 as a function of temperature. The photoconductivity σ is proportional to the product of the density of photoexcited free charges N and the mobility μ, following $\sigma = Ne\mu = (N_{abs\_vol}\phi)e\mu$, where $N_{abs\_vol,}$ ϕ and e represent the number of absorbed photons per volume, the photon-to-free-charge conversion quantum yield, and elementary charge, respectively. For a fair comparison between DNTT vs C8-DNTT-C8, the photoconductivity is normalised to N_{abs_vol}, or equivalently $\phi\mu$ (Eq. 1, see Methods), following beyond-bandgap excitation (by 3.1 eV pulses).
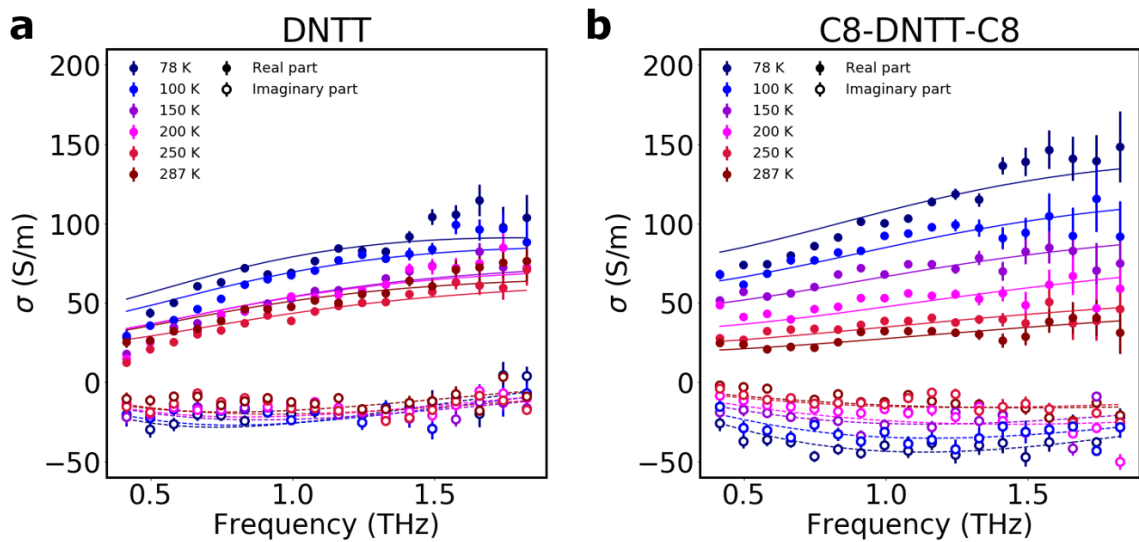
Figure 3: Frequency-dependent THz photoconductivity. The data were recorded 0.5 ps after excitation of **(a)** DNTT and **(b)** C8-DNTT-C8 samples with 50 fs pulses with a photon energy of 3.1 eV. The lines are fitting to the Drude-Anderson model described in the text (solid lines indicate the real part, and the dashed line the imaginary part of the conductivity). Error bars represent the error propagated from the standard error on the Fourier transform of the signals.

Table 1: Calculated electronic couplings H_{kl} for the nearest neighbor crystal pairs along different directions (Dir.), and values from literature (Lit.). All values in meV (except distances (Dist.) in Angstrom).

System	Dir.	Dist.	H_{kl}(POD)[a]	H_{kl}(AOM)[b]	H_{kl} Lit.	λ[c]
	P_a	6.187	87.4	80.0	84.8[d], 81[e]	
DNTT	T_1	5.148	21.5	26.9	37.2[d], 28[e]	134
	T_2	4.886	-117.9	-113.8	-119.0[d], -94[e]	
C8-DNTT-C8	P_a	5.987	93.1	83.6	78.9[d]	147
	T	4.941	-60.7	-56.2	-60.3[d]	

[a] Projection operator-based diabatization (POD) reference couplings are obtained as detailed in Supplementary Note 8. [b] Parametrized analytic overlap method (AOM) results are obtained as described in Supplementary Note 9. [c] Reorganization energies computed with Eq. 3 in the Supplementary Note 8. [d] All parameters refer to hole carriers. Taken from Ref.[29] (the unit-cell geometry was pre-optimized in this work[29]). [e] Taken from Ref.[31].
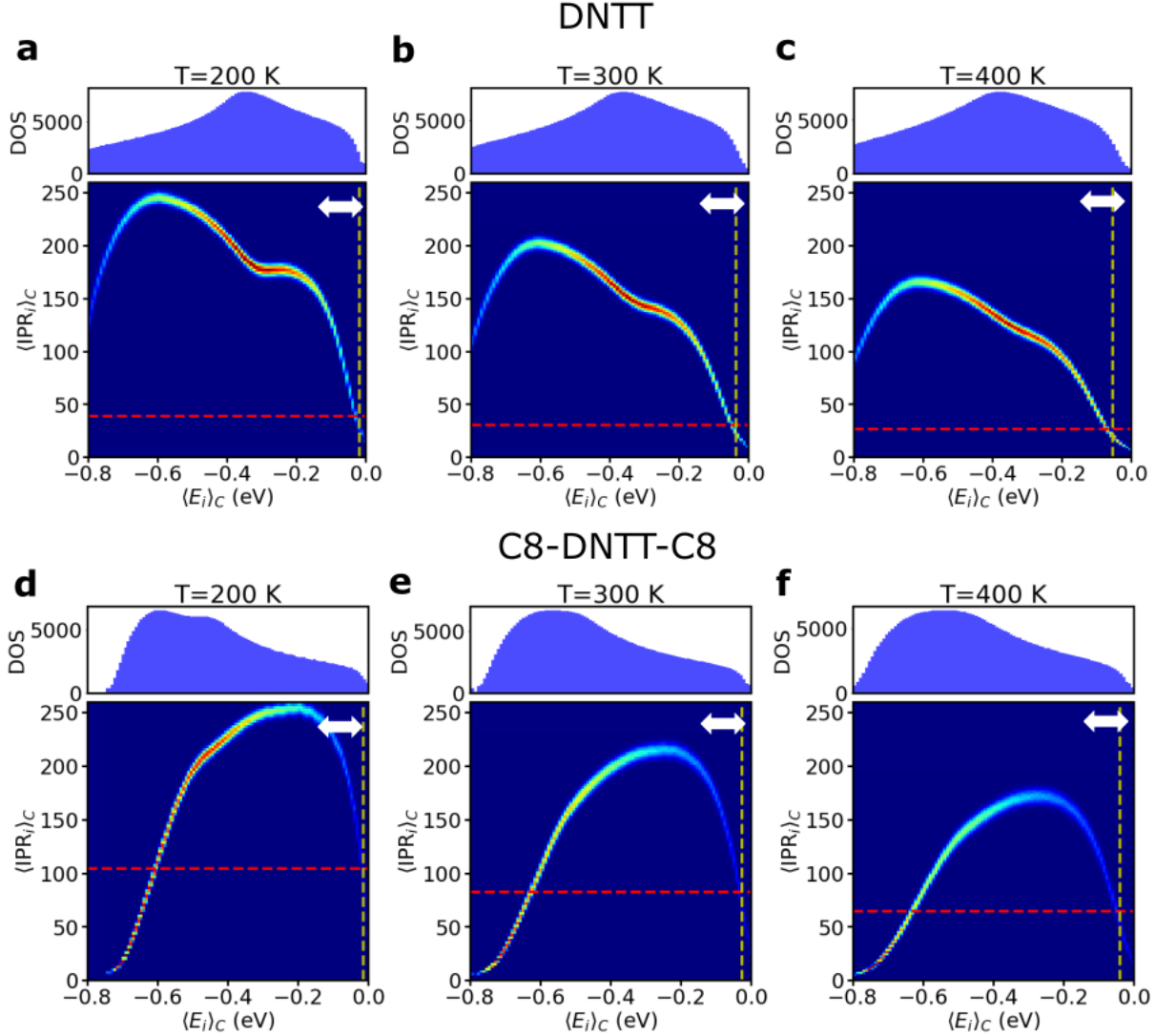
Figure 4: DOS and state-resolved inverse participation ratio ($\langle IPR_i \rangle_C$). Panels **(a),(b),(c)** refer to DNTT, while **(d),(e),(f)** to C8-DNTT-C8. Top figures depict the DOS at different temperatures (left to right: 200 K, 300 K, 400 K). Bottom panels display 2D histograms correlating the delocalization of the valence band states, quantified by the inverse participation ratio $\langle IPR_i \rangle_C$ (Eq. 5) versus their energies ($\langle E_i \rangle_C$). The states become denser going from regions colored in light-blue, to yellow to red (where the states are more concentrated). DOS and state-resolved IPR ($\langle IPR_i \rangle_C$) are computed from Hamiltonians extracted from around 200 FOB-SH trajectories (they include the effect of thermal disorder). Vertical dashed yellow lines indicate band active state energy a ($\langle E_a \rangle_C$) which increases with increasing thermal energy. Horizontal dashed red lines are used to indicate the Boltzmann average IPR of the valence band states ($\langle IPR \rangle_B$). Note how in DNTT the Boltzmann average IPR is weakly dependent on the temperature, while C8-DNTT-C8 it decreases comparably more strongly with increasing temperature.
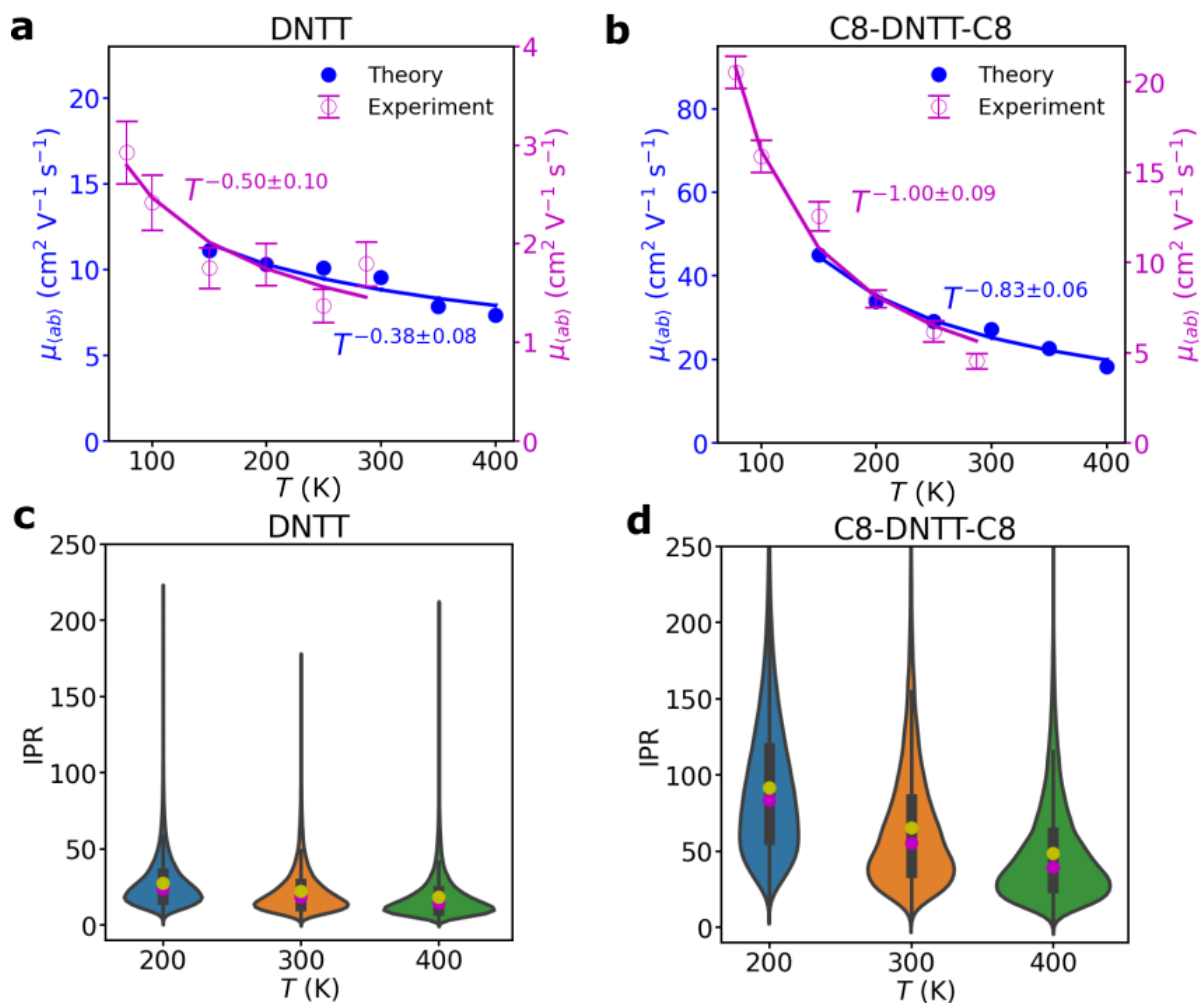
Figure 5: Temperature-dependent IPR and experimental and theoretical charge mobilities for DNTT and C8-DNTT-C8. **(a)** and **(b)** Experimental μ, obtained from Drude-Anderson model (magenta data) and theoretical μ of hole (blue data) as a function of temperature and related power-law fitting. Error bars represent the error propagated from the standard error on the fitting parameters (details in the Method section). Theoretical mobilities are given as an average over the *a* and *b* crystallographic directions of the herringbone layers of the two OSs as described in the text. The uncertainties obtained from the fitting is given for both theory and experiment. Panels **(c)** and **(d)** violin plots representing IPR distribution (obtained from 200 FOB-SH trajectories) as a function of temperature for DNTT and C8-DNTT-C8, respectively. Black bars in the center represent interquartile ranges, while the tinner black lines stretching from the center represent Tukey's fences. Magenta and yellow dots represent the median and mean of the distribution, respectively. The mode of the distributions can be inferred by their maximum width. Note that in C8-DNTT-C8 the IPR distributions have longer tails at all temperatures compared to DNTT and the average IPR decreases more strongly in C8-DNTT-C8 compared to DNTT, indicating more efficient quantum delocalization in the former system.

References

1. Oberhofer, H., Reuter, K. & Blumberger, J. Charge Transport in Molecular Materials: An Assessment of Computational Methods. *Chem. Rev.* **117**, 10319–10357 (2017).

2. Fratini, S., Mayou, D. & Ciuchi, S. The Transient Localization Scenario for Charge Transport in Crystalline Organic Materials. *Adv. Funct. Mater.* **26**, 2292–2315 (2016).

3. Troisi, A. Charge transport in high mobility molecular semiconductors: classical models and new theories. *Chem. Soc. Rev.* **40**, 2347 (2011).

4. Giannini, S. & Blumberger, J. Charge Transport in Organic Semiconductors: The Perspective from Nonadiabatic Molecular Dynamics. *Acc. Chem. Res.* **55**, 819–830 (2022).

5. Chang, J.-F. *et al.* Hall-Effect Measurements Probing the Degree of Charge-Carrier Delocalization in Solution-Processed Crystalline Molecular Semiconductors. *Phys. Rev. Lett.* **107**, 066601 (2011).

6. Sakanoue, T. & Sirringhaus, H. Band-like temperature dependence of mobility in a solution-processed organic semiconductor. *Nat. Mater.* **9**, 736–740 (2010).

7. Marumoto, K., Kuroda, S., Takenobu, T. & Iwasa, Y. Spatial Extent of Wave Functions of Gate-Induced Hole Carriers in Pentacene Field-Effect Devices as Investigated by Electron Spin Resonance. *Phys. Rev. Lett.* **97**, 256603 (2006).

8. Matsui, H., Mishchenko, A. S. & Hasegawa, T. Distribution of Localized States from Fine Analysis of Electron Spin Resonance Spectra in Organic Transistors. *Phys. Rev. Lett.* **104**, 056602 (2010).

9. Tsurumi, J. *et al.* Coexistence of ultra-long spin relaxation time and coherent charge transport in organic single-crystal semiconductors. *Nat. Phys.* **13**, 994–998 (2017).

10. Coropceanu, V. *et al.* Charge transport in organic semiconductors. *Chem. Rev.* **107**, 926–52 (2007).

11. Karl, N. Charge carrier transport in organic semiconductors. *Synth. Met.* **133**–**134**, 649–657 (2003).

12. Yi, H. T., Gartstein, Y. N. & Podzorov, V. Charge carrier coherence and Hall effect in organic semiconductors. *Sci. Rep.* **6**, 1–11 (2016).

13. Podzorov, V., Menard, E., Rogers, J. A. & Gershenson, M. E. Hall Effect in the Accumulation Layers on the Surface of Organic Semiconductors. *Phys. Rev. Lett.* **95**, 226601 (2005).

14. Jurchescu, O. D., Baas, J. & Palstra, T. T. M. Effect of impurities on the mobility of single crystal pentacene. *Appl. Phys. Lett.* **84**, 3061–3063 (2004).

15. Laarhoven, H. A. V. *et al.* On the mechanism of charge transport in pentacene. *J. Chem. Phys.* **129**, (2008).

16. Fratini, S., Nikolka, M., Salleo, A., Schweicher, G. & Sirringhaus, H. Charge transport in

high-mobility conjugated polymers and molecular semiconductors. *Nat. Mater.* **19**, 491–502 (2020).

17. Fratini, S. & Ciuchi, S. Bandlike Motion and Mobility Saturation in Organic Molecular Semiconductors. *Phys. Rev. Lett.* **103**, 266601 (2009).

18. Mott, S. N. The mobility edge since 1967. in *J. Phys. C: Solid State Phys.* 657–684 (1995). doi:10.1142/9789812794086_0042.

19. Ciuchi, S., Fratini, S. & Mayou, D. Transient localization in crystalline organic semiconductors. *Phys. Rev. B* **83**, 081202 (2011).

20. Fratini, S., Ciuchi, S., Mayou, D., de Laissardière, G. T. & Troisi, A. A map of high-mobility molecular semiconductors. *Nat. Mater.* **16**, 998–1002 (2017).

21. Nematiaram, T., Padula, D., Landi, A. & Troisi, A. On the Largest Possible Mobility of Molecular Semiconductors and How to Achieve It. *Adv. Funct. Mater.* **30**, 2001906 (2020).

22. Nelson, T. R. *et al.* Non-adiabatic Excited-State Molecular Dynamics: Theory and Applications for Modeling Photophysics in Extended Molecular Materials. *Chem. Rev.* **120**, 2215–2287 (2020).

23. Xie, W., Holub, D., Kubař, T. & Elstner, M. Performance of Mixed Quantum-Classical Approaches on Modeling the Crossover from Hopping to Bandlike Charge Transport in Organic Semiconductors. *J. Chem. Theory Comput.* **16**, 2071–2084 (2020).

24. Wang, L., Qiu, J., Bai, X. & Xu, J. Surface hopping methods for nonadiabatic dynamics in extended systems. *WIREs Comput. Mol. Sci.* **10**, e1435 (2020).

25. Giannini, S. *et al.* Quantum localization and delocalization of charge carriers in organic semiconducting crystals. *Nat. Commun.* **10**, 3843 (2019).

26. Giannini, S., Carof, A., Ellis, M., Ziogos, O. G. & Blumberger, J. Chapter 6. From Atomic Orbitals to Nano-scale Charge Transport with Mixed Quantum/Classical Non-adiabatic Dynamics: Method, Implementation and Application. in 172–202 (2021). doi:10.1039/9781839164668-00172.

27. Peng, B., He, Z., Chen, M. & Chan, P. K. L. Ultrahigh On-Current Density of Organic Field-Effect Transistors Facilitated by Molecular Monolayer Crystals. *Adv. Funct. Mater.* **32**, 2202632 (2022).

28. Mitsui, C. *et al.* High-Performance Solution-Processable N-Shaped Organic Semiconducting Materials with Stabilized Crystal Phase. *Adv. Mater.* **26**, 4546–4551 (2014).

29. Schweicher, G. *et al.* Chasing the "Killer" Phonon Mode for the Rational Design of Low-Disorder, High-Mobility Molecular Semiconductors. *Adv. Mater.* **31**, 1902407 (2019).

30. Xi, J., Long, M., Tang, L., Wang, D. & Shuai, Z. First-principles prediction of charge mobility in carbon and organic nanomaterials. *Nanoscale* **4**, 4348–4369 (2012).

31. Sánchez-Carrera, R. S., Atahan, S., Schrier, J. & Aspuru-Guzik, A. Theoretical

characterization of the air-stable, high-mobility dinaphtho[2,3-b:2'3'-f]thieno[3,2-b]-thiophene organic semiconductor. *J. Phys. Chem. C* **114**, 2334–2340 (2010).

32. Sokolov, A. N. *et al.* From computational discovery to experimental characterization of a high hole mobility organic crystal. *Nat. Commun.* **2**, 437 (2011).

33. Rußegger, N. *et al.* Molecular Charge Transfer Effects on Perylene Diimide Acceptor and Dinaphthothienothiophene Donor Systems. *J. Phys. Chem. C* **126**, 4188–4198 (2022).

34. Xie, W. *et al.* Temperature-independent transport in high-mobility dinaphtho-thieno-thiophene (DNTT) single crystal transistors. *Adv. Mater.* **25**, 3478–3484 (2013).

35. Huang, Y. *et al.* Effectively modulating thermal activated charge transport in organic semiconductors by precise potential barrier engineering. *Nat. Commun.* **12**, 21 (2021).

36. Ulbricht, R., Hendry, E., Shan, J., Heinz, T. F. & Bonn, M. Carrier dynamics in semiconductors studied with time-resolved terahertz spectroscopy. *Rev. Mod. Phys.* **83**, 543–586 (2011).

37. Hoberg, C., Balzerowski, P., Ockelmann, T. & Havenith, M. Ultrafast Solvation Dynamics Probed by Optical-Pump THz-Probe Spectroscopy. *Int. Conf. Infrared, Millimeter, Terahertz Waves, IRMMW-THz* **2018**-**Septe**, (2018).

38. Jepsen, P. U., Cooke, D. G. & Koch, M. Terahertz spectroscopy and imaging - Modern techniques and applications. *Laser Photonics Rev.* **5**, 124–166 (2011).

39. Glover, R. E. & Tinkham, M. Transmission of Superconducting Films at Millimeter-Microwave and Far Infrared Frequencies. *Phys.Rev.* **104**, 844–845 (1956).

40. Huggard, P. G. *et al.* Drude conductivity of highly doped GaAs at terahertz frequencies. *J. Appl. Phys.* **87**, 2382–2385 (2000).

41. Fratini, S., Ciuchi, S. & Mayou, D. Phenomenological model for charge dynamics and optical response of disordered systems: Application to organic semiconductors. *Phys. Rev. B* **89**, 235201 (2014).

42. Li, Z. Q. *et al.* Light Quasiparticles Dominate Electronic Transport in Molecular Crystal Field-Effect Transistors. *Phys. Rev. Lett.* **99**, 016403 (2007).

43. Fischer, M., Dressel, M., Gompf, B., Tripathi, A. K. & Pflaum, J. Infrared spectroscopy on the charge accumulation layer in rubrene single crystals. *Appl. Phys. Lett.* **89**, 1–4 (2006).

44. Yada, H. *et al.* Carrier dynamics of rubrene single-crystals revealed by transient broadband terahertz spectroscopy. *Appl. Phys. Lett.* **105**, 143302 (2014).

45. Harrelson, T. F. *et al.* Direct probe of the nuclear modes limiting charge mobility in molecular semiconductors. *Mater. Horizons* **6**, 182–191 (2019).

46. Sleigh, J. P., McMahon, D. P. & Troisi, A. Effect of the intermolecular thermal motions on the tail of the electronic density of states in polyacene crystals. *Appl. Phys. A Mater. Sci. Process.* **95**, 147–152 (2009).

47.   Giannini, S., Ziogos, O. G., Carof, A., Ellis, M. & Blumberger, J. Flickering Polarons Extending over Ten Nanometres Mediate Charge Transport in High-Mobility Organic Crystals. *Adv. Theory Simulations* **3**, 2070021 (2020).

48.   Carof, A., Giannini, S. & Blumberger, J. How to calculate charge mobility in molecular materials from surface hopping non-adiabatic molecular dynamics-beyond the hopping/band paradigm. *Phys. Chem. Chem. Phys.* **21**, 26368–26386 (2019).

49.   Ghosh, S., Giannini, S., Lively, K. & Blumberger, J. Nonadiabatic dynamics with quantum nuclei: simulating charge transfer with ring polymer surface hopping. *Faraday Discuss.* **221**, 501–525 (2020).

50.   Carof, A., Giannini, S. & Blumberger, J. Detailed balance, internal consistency, and energy conservation in fragment orbital-based surface hopping. *J. Chem. Phys.* **147**, 214113 (2017).

51.   Jiang, Y. *et al.* Nuclear quantum tunnelling and carrier delocalization effects to bridge the gap between hopping and bandlike behaviors in organic semiconductors. *Nanoscale Horizons* **1**, 53–59 (2016).

52.   Shuai, Z., Li, W., Ren, J., Jiang, Y. & Geng, H. Applying Marcus theory to describe the carrier transports in organic semiconductors: Limitations and beyond. *J. Chem. Phys.* **153**, 080902 (2020).

53.   Li, W., Ren, J. & Shuai, Z. A general charge transport picture for organic semiconductors with nonlocal electron-phonon couplings. *Nat. Commun.* **12**, 4260 (2021).

54.   Munn, R. W. & Silbey, R. Theory of electronic transport in molecular crystals. II. Zeroth order states incorporating nonlocal linear electron–phonon coupling. *J. Chem. Phys.* **83**, 1843–1853 (1985).

55.   Giannini, S., Carof, A. & Blumberger, J. Crossover from Hopping to Band-Like Charge Transport in an Organic Semiconductor Model: Atomistic Nonadiabatic Molecular Dynamics Simulation. *J. Phys. Chem. Lett.* **9**, 3116–3123 (2018).

Methods

Materials and sample preparation Dinaphtho[2,3-b:2′,3′-f]thieno[3,2-b]-thiophene (DNTT, Sigma Aldrich, 99% purity) was used as received. C8-DNTT-C8 was synthesized according to previously described procedures.[56] The DNTT films and C8-DNTT-C8 films were prepared by organic molecular beam deposition in an ultra-high vacuum chamber with a base pressure of 10^{-8} mbar. For deposition each compound was resistively heated in crucibles in Knudsen-cells and the deposition rate and film thickness was monitored during preparation by a quartz crystal microbalance (QCM), calibrated using X-ray reflectivity (XRR) measurements. DNTT films of 240nm thickness and C8-DNTT-C8 films of 100nm and 500nm thickness were prepared over 1 cm^2 fused silica substrates with a growth rate of 20 Å/min.

Optical Pump Terahertz (THz) Probe Spectroscopy. The details of the THz setup are described in Ref.[57]. Briefly, we operate the THz spectrometer by Ti:sapphire amplified pulsed laser system (with the following output features: 800 nm central wavelength, duration of ~50 fs and a repetition rate of 1 kHz. The THz field is generated using optical rectification in a ZnTe crystal (along <110> orientation). The THz field transmitted through the sample is measured in the time domain at a chosen delay time, using electro-optical sampling in a second ZnTe crystal. The bandwidth of the THz pulse is ~ 2 THz. Optical excitations of the OS samples are conducted by 400 nm pulses, which are generated by second harmonic generation in a BBO crystal. The conductivity of pump-induced charge carriers was studied by measuring the THz absorption induced by photoinjected charges. Specifically, we monitored the peak absorption of the THz field ($\Delta E = E_{pump} - E$) by fixing the sampling beam as a function of the relative arrival between the pump and the probe, i.e, the pump-probe delay time. We then infer the mobility as a function of pump-probe delay time, *i.e.* $\phi\mu$, by applying the thin film approximation [39] (more details can be found in Supplementary Note 2) following:

$$\frac{\sigma}{N_{abs\_vol}} = \left(-\frac{\varepsilon_0 c \left(n_{sub} + n_{air}\right)}{l} \cdot \frac{\Delta E}{E} \right) \frac{l}{N_{abs}} = \frac{Ne\mu}{N_{abs\_vol}} \propto \phi\mu \qquad (1)$$

Where N_{abs} is the absorbed sheet photon density, $n_{sub} = 1.96$ is the THz refractive index of fused silica, n_{air} (~1) the refractive index of the air and l the thickness of the OS films. N_{abs} is obtained as the product of the incident photon density and the absorbance percentage. N_{abs_vol} is the number of absorbed photons per volume. During the temperature dependence OPTP measurements, the samples were placed inside a cryostat under vacuum conditions ($< 2 \times 10^{-4}$ mbar). Importantly, due to the transient nature (~ 1 ps duration) of the THz pulses, the charge carriers are driven over a short length scale (~ 10 nm), minimizing the probability of charge carriers interacting with defects, thereby making THz spectroscopy ideal for studying intrinsic local charge carrier mobility in OS films. This technique has been widely applied to understanding charge transport effects in inorganic[40] and in high mobility organic semiconductors[44,58] (in both thin-film[59] and dispersion geometries[60]).

Drude-Anderson model. This model was derived in Ref.[41] by Fratini *et al.* to account for the suppression of the conductivity, $\sigma(\nu)$, in the low frequency range due to the presence of dynamical disorder induced by thermal intermolecular vibrations. The Drude-Anderson (DA) model

describes transport of transiently localized charge carriers involving three different time regimes. Initially, diffusive transport of free carriers occurs following semiclassical Boltzmann theory with an elastic scattering time τ. Then, a second time scale $\tau_b (> \tau)$ sets in that accounts for "backscattering" events leading to localization of charges due to molecular disorder. The dynamical nature of thermal disorder is included via a third, longer time scale, τ_{in}, which is inversely proportional to the frequency of the molecular vibrations coupled to the charge carrier. The DA model describes transport of charges that are subject to localization (due to backscattering events), but that can further diffuse over a distance L, called localization length, with a rate $1/\tau_{in}$, owing to molecular vibrations that can trigger charge diffusion and mobility (see Eq. 4).[41] In essence, the DA model generalizes other phenomenological models used to fit the photoconductivity response by addressing localization/delocalization induced by dynamic disorder. Most importantly, DA goes beyond the Drude-Smith model[61,62] that was derived to describe charge carrier localization effects from static disorder (see a discussion of the latter model in Supplementary Note 6).

The Drude-Anderson formula reads:

$$\sigma(v) = \frac{Ne^2 L^2}{\tau_b - \tau} \frac{\tanh\left(\frac{hv}{2k_B T}\right)}{hv} \left(\frac{1}{1 + \frac{\tau}{\tau_{in}} - i2\pi v\tau} - \frac{1}{1 + \frac{\tau_b}{\tau_{in}} - i2\pi v\tau_b} \right) \tag{2}$$

Where τ represents the elastic scattering, τ_b is the backscattering time ($\tau_b > \tau$), introduced to describe electron localization at longer times, and τ_{in} is the inelastic time related to the slow intermolecular motion responsible for the suppression of the long-time backscattering restoring charge carrier diffusion.[41] According to this model, besides the three different time scales, the product NL^2 between the density of charges (N) and the localization length (L^2), constitutes an additional fitting parameter.

In Fig 3, we have fitted the photoconductivity data with the DA formula in Eq. 3 following the procedure outlined in Ref.[44]. Particularly, to limit the number of free parameters, we set τ/τ_b to 0.1. We have checked that changing this ratio between 0.1 and 0.01 does not appreciably affect the results. We have also set τ_{in} to be a globally shared parameter at all temperature because it is a material property that can be assumed independent of temperature.[44] We verified the quality of this assumption in Supplementary Fig. 27 by explicitly computing the power spectral density of the electronic coupling fluctuations directly affected by intermolecular nuclear vibrations. We also verified that even leaving it as free parameter, τ_{in} does not change significantly with temperature. To extract N from the product NL^2 we assumed that L^2 can be replaced by L_{th}^2 calculated from TLT simulations with Eq. 11 in Supplementary Note 23. We refer to N calculated from the Drude-Anderson model in this manner, as N_{DA}. We estimated this value to be $N_{DA} = 1.4 \cdot 10^{18}$ cm^{-3} and $3.8 \cdot 10^{17}$ cm^{-3} in DNTT and C8-DNTT-C8, respectively, when averaged over all temperatures (see Supplementary Table 1). As an additional validation that N remains substantially temperature independent we also calculated this value using the Drude-Smith fitting of our data (N_{DS}) (as detailed in the Supplementary Note 6).

The DA model[41] allows to recover the necessary parameters to calculate the dc conductivity in the limit $v \to 0$ as:

$$\sigma_{dc}(T) \cong \frac{Ne^2}{k_{\mathrm{B}}T}\frac{L^2}{2\tau_{in}} \tag{3}$$

and so, the mobility in the dilute density carrier's regime becomes:

$$\mu = \frac{\sigma_{dc}}{Ne} \cong \frac{e}{k_{\mathrm{B}}T}\frac{L^2}{2\tau_{in}} \tag{4}$$

From the comparison between Eq. 3 and Eq. 10 below, it is easy to see that the diffusion coefficient can be written as $D \cong \frac{L^2}{2\tau_{in}}$.

FOB-SH non-adiabatic molecular dynamics of hole transport. When it comes to the study of application-relevant nano-scale systems, mixed quantum-classical non-adiabatic dynamics, using either a fully atomistic[4,47] or a coarse-grained description of the nuclear degrees of freedom,[24,63] have proven to be extremely powerful to accurately propagate charge carriers[25,47,63] or excitons[64–67] in OSs. The advantage of non-perturbative algorithms is that no limiting assumptions on the actual charge carrier dynamics need to be introduced, as the coupled charge-nuclear motion is solved explicitly in real-time. The wavefunction undergoes (transient) quantum (de)localization along its time-dependent dynamics, passing from localized to more delocalized states under the influence of thermal motion. Among various techniques, FOB-SH stands out as a fully atomistic mixed quantum-classical approach that allows propagating the electron-nuclear motion in real-time for large nano-scale systems. The FOB-SH methodology has been described in detail in previous works.[4,26,47,48] Here, we only give a very brief summary of the relevant equations. As common to many OSs,[4] the valence band of DNTT and C8-DNTT-C8 is well described by the following one-particle Hamiltonian (as verified in Supplementary Fig. 17):

$$H(t) = \sum_k^M \epsilon_k(t)|\phi_k\rangle\langle\phi_k| + \sum_{k \neq l}^M H_{kl}(t)|\phi_k\rangle\langle\phi_l| \tag{5}$$

where $\phi_k = \phi_k(\boldsymbol{R}(t))$ is the (orthogonalized) HOMO of molecule k for hole transport, $\boldsymbol{R}(t)$, are the time-dependent nuclear coordinates, $\epsilon_k(t) = \epsilon_k(\boldsymbol{R}(t))$ is the site energy, that is, the potential energy of the state with the hole located at site k, and $H_{kl}(t) = H_{kl}(\boldsymbol{R}(t))$ is the electronic coupling between ϕ_k and ϕ_l. The Hamiltonian in Eq. 5 represents the core of the FOB-SH method. All Hamiltonian matrix elements, that is, site energies and couplings, depend on the nuclear coordinates, which, in turn, depend on time, as determined by the nuclear (molecular) dynamics. To open up applications to large super-cell sizes, necessary to accurately compute charge transport properties in high-mobility OSs, the Hamiltonian matrix elements are calculated on-the-fly using a combination of parametrized classical force-fields for site energies[47] and a very efficient analytic overlap method (AOM)[68,69] for the computation of the electronic couplings. A full description of the technical details and reference calculations needed is given in Supplementary Note 9.

Concerning the propagation of the coupled electron-nuclear motion, FOB-SH relies on a swarm of classical trajectories which, according to Tully's algorithm,[70] approximate the evolution of a quantum wavepacket. In FOB-SH the hole carrier associated with each of the classical trajectories is described by a time-dependent one-particle wavefunction, $\Psi(t)$, expanded in the same (localized) basis that is used to represent the Hamiltonian Eq. 5,

$$\Psi(t) = \sum_{l}^{M} u_l(t)\phi_l(\boldsymbol{R}(t)) \tag{6}$$

where u_l are the expansion coefficients. The time-evolution of the wavefunction is obtained by solving the time-dependent Schrödinger equation, which, using $\Psi(t)$ Eq. 6, becomes:

$$i\hbar\dot{u}_k(t) = \sum_{l}^{M} u_l(t)(H_{kl}(\boldsymbol{R}(t)) - i\hbar d_{kl}(\boldsymbol{R}(t))) \tag{7}$$

where $d_{kl} = \langle\phi_k|\dot{\phi}_l\rangle$ are the non-adiabatic coupling elements. The nuclear degrees of freedom are propagated according to Newton's equation of motion on one of the potential energy surfaces (PES), ψ_a, obtained by diagonalizing the Hamiltonian Eq. 5 and denoted as E_a (a indicates active surface). The nuclear motion couples to the motion of the charge carrier via the dependences on $\boldsymbol{R}(t)$ in Eq. 7, resulting in diagonal and off-diagonal electron-phonon coupling. Notably, the coupling (or feedback) from the charge to the nuclear motion is accounted for by transitions of the nuclear dynamics ("hops") from the PES of the active eigenstate a to the PES of another eigenstate j using Tully's surface hopping probability.[70] A detailed description of the algorithm is given in Ref.[26] FOB-SH is used in combination with some important extensions of the original surface hopping method[70] that are necessary for accurate dynamics: decoherence correction, removal of decoherence correction induced artificial long-range charge transfers, tracking of trivial surface crossings, and adjustment of the velocities in the direction of the nonadiabatic coupling vector in the case of a successful surface hop. We refer to Refs.[26,48,50,55] for a detailed description and discussion of the importance of these additions to the original fewest switches surface hopping method.[70]

Delocalization and mean squared displacement. A common measure used to quantify the delocalization of a given eigenstate ψ_i of the Hamiltonian in Eq. 5, is the inverse participation ratio (IPR$_i$):

$$\text{IPR}_i(t) = \frac{1}{N_{\text{traj}}} \sum_{n=1}^{N_{\text{traj}}} \frac{1}{\sum_k^M \left|U_{ki}^{(n)}(t)\right|^4} \tag{8}$$

where $U_{ki}^{(n)}(t)$ are the components of the eigenvector ψ_i (*i.e.* adiabatic state i), in trajectory n at a given time t. Note that ψ_i can be represented in terms of the localized site basis, by $\psi_i = \sum_k^M U_{ki}\phi_k$. The numerical value of the IPR represents the number of molecules (sites) ψ_i is delocalized over. In Fig. 4, this quantity is averaged over time steps (*i.e.* configurations) to give $\langle\text{IPR}_i\rangle_{\text{C}}$ and plotted against the energy of a given state i, averaged over configurations, $\langle E_i\rangle_{\text{C}}$. IPR$_i$

can also be Boltzmann energy weighted to give a thermal average IPR, indicated in the text as $\langle \text{IPR} \rangle_\text{B}$.

A similar definition can be used to describe the delocalization of the carrier wavefunction $\Psi(t)$, obtained by directly solving Eq. 7 along time. In this case, the IPR becomes:

$$\text{IPR}(t) = \frac{1}{N_{traj}} \sum_{n=1}^{N_\text{traj}} \frac{1}{\sum_k^M \left| u_k^{(n)}(t) \right|^4} \tag{9}$$

where $u_k^{(n)}(t)$ are the expansion coefficients of the wavefunction in Eq. 6 at a given time t, in trajectory n. The latter definition can be averaged over time to get an average charge carrier size ($\langle \text{IPR} \rangle$). We note at this point that Eq. 8 and 9 are equivalent only when the wavefunction of the system is a pure state (*i.e.*, an adiabatic state i of the system). Although, quantum decoherence pushes the wavefunction to resemble an adiabatic state, generally it remains a superposition of several adiabatic states with different weights. Eq. 9 takes this mixing into account and is more general in characterizing the charge carrier size (and less affected by sudden changes in wavefunction character and trivial crossings[48]).

The solution of Eq. 7 gives also the possibility to compute the charge carrier mobility tensor $\mu_{\alpha\beta}$ (where α (β) represent Cartesian coordinates, *x, y, z*) as a function of temperature. In particular,

$$\mu_{\alpha\beta} = \frac{e D_{\alpha\beta}}{k_\text{B} T} \tag{10}$$

e is the elementary charge, k_B the Boltzmann constant and T the temperature. In this work, the crystallographic directions of the plane *a* and *b* of DNTT and C8-DNTT-C8 (which are both monoclinic) were chosen parallel to the Cartesian coordinates *x* and *y*. In this representation, the off-diagonal components of the mobility tensor are zero due to symmetry, and one can consider just the diagonal tensor components (along *a* and *b* crystallographic directions).

The diffusion tensor components, $D_{\alpha\beta} = \frac{1}{2} \lim_{t\to\infty} \frac{d\text{MSD}_{\alpha\beta}(t)}{dt}$, can be obtained as the time derivative of the mean squared displacement along the nine Cartesian components ($\text{MSD}_{\alpha\beta}$),

$$\text{MSD}_{\alpha\beta} = \frac{1}{N_{traj}} \sum_{n=1}^{N_{traj}} \left\langle \Psi^{(n)}(t) \middle| (\alpha - \alpha_{0,n})(\beta - \beta_{0,n}) \middle| \Psi^{(n)}(t) \right\rangle \tag{11}$$

where $\alpha_{0,n}$ ($\beta_{0,n}$) are the initial positions of the center of charge in trajectory n, $\alpha_{0,n} = \left\langle \Psi^{(n)}(0) \middle| \alpha \middle| \Psi^{(n)}(0) \right\rangle$.

Simulation details. The simulation protocol employed in this work broadly follows the one devised in our previous works.[25,47] For both DNTT and C8-DNTT-C8, a series of supercells of

increasing size were built from the experimental crystallographic unit cell. The dimensions of the largest supercells constructed are summarized in the Supplementary Table 2. These supercells were equilibrated in periodic boundary conditions for the neutral state at 150 K, 200 K, 250 K, 300 K, 350 K and 400 K for 500 ps in the NVT ensemble using a Nosé-Hoover thermostat. This step was followed by at least 250 ps equilibration in the NVE ensemble. In both cases, a nuclear time step of $\Delta t = 1$ fs was used. From the NVE trajectories an uncorrelated set of positions and velocities were chosen as starting configurations for FOB-SH simulations. About a thousand molecules of DNTT and C8-DNTT-C8 within their respective rectangular region of the $a - b$ high mobility plane were treated as electronically active, that is, their HOMO orbitals were used as molecular sites for construction of the electronic Hamiltonian in Eq. 5 (see Supplementary Table 2). All other molecules of the supercell were treated electronically inactive and interacted with the active region only via non-bonded interactions. FOB-SH non-adiabatic dynamics simulations were carried out with a much smaller nuclear time step compared to the standard MD equilibration step (*i.e.* $\Delta t = 0.05$ fs for DNTT and $\Delta t = 0.1$ fs for C8-DNTT). The electronic time step for integration of Eq. 7 using the Runge–Kutta algorithm to 4th order was 5 times smaller than the nuclear time step ($\delta t = \Delta t / 5$). The small nuclear time steps used in FOB-SH were necessary to efficiently tackle trivial crossings and to achieve an accurate dynamic. Additionally, all FOB-SH simulations applied a state-tracking for an automatic detection of trivial crossings and a projection algorithm for removal of decoherence correction-induced artificial long-range charge transfer.[26,47,48] For each of both systems from about 200 to 300 classical trajectories of length 0.8 to 1 ps, depending on the size of the systems, were run to extract the MSD (Eq. 11) and related mobility values for all 5 different temperatures. For each temperature, the in-plane mobility ($\mu_{\langle ab \rangle}$) was calculated and averaged over at least two different supercell sizes to reduce numerical uncertainty as much as possible (see Supplementary Table 7). Convergence of the mobilities of both systems as a function of system size has been checked and reported in Supplementary Fig. 24. The initial carrier wavefunction is chosen to be localized on a single active molecule *m*, $\Psi(0) = \phi_m$ and propagated in time according to the surface hopping algorithm in the NVE ensemble. Notably, even though the short-time relaxation dynamics of the wavefunction (which is a linear combination of the valence band states) depends on the choice of the initial condition, the long-time diffusive dynamics, diffusion constant and average IPR (Eq. 9) are the same for different initial states. This is because FOB-SH fulfils detailed balance to a very good approximation thanks to the adjustment of the velocities in the direction of the non-adiabatic coupling vector.[26,50] This essential condition, together with a decoherence correction[38], ensure that the populations of the valence band states reach thermal equilibrium at long times and avoid the infinite temperature problem of the Ehrenfest dynamics. All simulations were carried out with our in-house implementation of FOB-SH in the CP2K simulation package.[71]

Data availability

The datasets generated during and/or analyzed during the current study are available in the Zenodo repository, https://zenodo.org/record/8109807 . The full data for this study totals a couple of TB and it is in cold storage accessible by the corresponding authors and available upon reasonable request.

Code availability

The custom codes used for this study are available from the corresponding authors upon request.

References

56. Kang, M. J. *et al.* Alkylated Dinaphtho[2,3-b:2′,3′-f]Thieno[3,2-b]Thiophenes (Cn-DNTTs): Organic Semiconductors for High-Performance Thin-Film Transistors. *Adv. Mater.* **23**, 1222–1225 (2011).

57. Beard, M. C., Turner, G. M. & Schmuttenmaer, C. A. Terahertz spectroscopy. *J. Phys. Chem. B* **106**, 7146–7159 (2002).

58. Yada, H. *et al.* Evaluating intrinsic mobility from transient terahertz conductivity spectra of microcrystal samples of organic molecular semiconductors. *Appl. Phys. Lett.* **115**, 143301 (2019).

59. D'Angelo, F., Mics, Z., Bonn, M. & Turchinovich, D. Ultra-broadband THz time-domain spectroscopy of common polymers using THz air photonics. *Opt. Express* **22**, 12475 (2014).

60. Wang, Z. Y. *et al.* Correlating Charge Transport Properties of Conjugated Polymers in Solution Aggregates and Thin-Film Aggregates. *Angew. Chemie - Int. Ed.* **60**, 20483–20488 (2021).

61. Smith, N. V. Drude theory and the optical properties of liquid mercury. *Phys. Lett. A* **26**, 126–127 (1968).

62. Smith, N. Classical generalization of the Drude formula for the optical conductivity. *Phys. Rev. B* **64**, 155106 (2001).

63. Wang, L., Prezhdo, O. V & Beljonne, D. Mixed quantum-classical dynamics for charge transport in organics. *Phys Chem Chem Phys* **17**, 12395–12406 (2015).

64. Giannini, S. *et al.* Exciton transport in molecular organic semiconductors boosted by transient quantum delocalization. *Nat. Commun.* **13**, 2755 (2022).

65. Sneyd, A. J., Beljonne, D. & Rao, A. A New Frontier in Exciton Transport: Transient Delocalization. *J. Phys. Chem. Lett.* **13**, 6820–6830 (2022).

66. Sneyd, A. J. *et al.* Efficient energy transport in an organic semiconductor mediated by transient exciton delocalization. *Sci. Adv.* **7**, eabh4232 (2021).

67. Prodhan, S., Giannini, S., Wang, L. & Beljonne, D. Long-Range Interactions Boost Singlet Exciton Diffusion in Nanofibers of π-Extended Polymer Chains. *J. Phys. Chem. Lett.* 8188–8193 (2021) doi:10.1021/acs.jpclett.1c02275.

68. Gajdos, F. *et al.* Ultrafast estimation of electronic couplings for electron transfer between pi;-conjugated organic molecules. *J. Chem. Theory Comput.* **10**, 4653–4660 (2014).

69. Ziogos, O. G. & Blumberger, J. Ultrafast estimation of electronic couplings for electron

transfer between pi-conjugated organic molecules. II. *J. Chem. Phys.* **155**, 244110 (2021).

70. Tully, J. C. Molecular dynamics with electronic transitions. *J. Chem. Phys.* **93**, 1061–1071 (1990).

71. Kühne, T. D. *et al.* CP2K: An electronic structure and molecular dynamics software package -Quickstep: Efficient and accurate electronic structure calculations. *J. Chem. Phys.* **152**, (2020).

Additional information

Supplementary information. The online version contains supplementary material available at [TO ADD].

Correspondence and requests for materials should be addressed to D.B. (david.beljonne@umons.ac.be), S.G. (samuele.giannini@umons.ac.be), M.Bonn. (bonn@mpip-mainz.mpg.de) and H.I.W. (h.wang5@uu.nl)